

Null stream analysis of Pulsar Timing Array data: localisation of resolvable gravitational wave sources

Janna Goldstein^{1*}, John Veitch^{1,2}, Alberto Sesana¹ & Alberto Vecchio¹

¹ School of Physics and Astronomy and Institute for Gravitational Wave Astronomy, University of Birmingham, Edgbaston B15 2TT, United Kingdom

² Institute for Gravitational Research, University of Glasgow, Glasgow, G12 8QQ, United Kingdom

ABSTRACT

Super-massive black hole binaries are expected to produce a gravitational wave (GW) signal in the nano-Hertz frequency band which may be detected by pulsar timing arrays (PTAs) in the coming years. The signal is composed of both stochastic and individually resolvable components. Here we develop a generic Bayesian method for the analysis of resolvable sources based on the construction of ‘null-streams’ which cancel the part of the signal held in common for each pulsar (the Earth-term). For an array of N pulsars there are $N - 2$ independent null-streams that cancel the GW signal from a particular sky location. This method is applied to the localisation of quasi-circular binaries undergoing adiabatic inspiral. We carry out a systematic investigation of the scaling of the localisation accuracy with signal strength and number of pulsars in the PTA. Additionally, we find that source sky localisation with the International PTA data release one is vastly superior than what is achieved by its constituent regional PTAs.

Key words: black hole physics - gravitational waves - pulsars: general

1 INTRODUCTION

The recent successes of the LIGO-Virgo collaboration (Abbott et al. 2016b,a, 2017) brought gravitational wave (GW) astronomy in the spotlight. Despite their great achievements, ground based interferometers are only sensitive in a frequency range from about 10 Hz to 1000 Hz and are thus suited for detection of stellar mass compact objects such as stellar mass black holes or neutron stars (Abadie et al. 2010). The GW spectrum however, extends for several more decades in frequency (Colpi & Sesana 2017). In particular, the low frequency band, is expected to be dominated by GW signals coming from a class of much more massive astrophysical sources: supermassive black hole binaries (SMBHBs, Begelman et al. 1980).

The adiabatic inspiral of $10^8 - 10^{10} M_{\odot}$ SMBHBs at cosmological distances generates loud GWs in the nHz-to- μ Hz frequency range (see, e.g., Sesana et al. 2008), where ground based interferometers are completely deaf. Fortunately, Nature provided us with formidably stable natural clocks that might allow to hear such low frequency waves in the foreseeable future: millisecond pulsars (MSPs, Lorimer 2008). Located at kpc distances within the Galaxy, MSPs behave like cosmic lighthouses sending periodic radio signals to the Earth. If a GW crosses the path of the radio photons, their null geodesic is modified, effectively resulting in a GW induced redshift (Sazhin 1978). In practice radio pulses arrive on Earth a little bit earlier or later than expected, an effect that can be measured if the time of arrivals (TOAs) of the radio pulses can be determined with enough precision. The TOAs of the most stable MSPs can be currently determined with an uncertainty of about 100ns (Verbiest et al.

2016), an accuracy level approaching the expected delays induced by the most massive SMBHBs populating the Universe (Sesana et al. 2009).

SMBHBs are expected to be common in the Universe, and pulsar timing arrays (PTAs) will be mostly sensitive to the incoherent superposition of GWs coming from the large population of these cosmological sources (Rajagopal & Romani 1995; Jaffe & Backer 2003; Sesana et al. 2008). At the high mass end and for sufficiently high frequencies however, SMBHBs become sparser, and the loudest ones will likely be individually detectable as deterministic sources (Sesana et al. 2009). Consequently, several algorithms and pipelines have been assembled in recent years to detect and characterize both a stochastic GW background and individual deterministic sources (see Perrodin & Sesana 2017, for a recent review). In both cases the challenge is to determine whether the data are better described by noise only or noise plus some GW signal. No GW detection has been reported thus far, and several pipelines have been used to produce upper limits on the strength of each type of source (Arzoumanian et al. 2014; Zhu et al. 2014; Shannon et al. 2015; Lentati et al. 2015; Taylor et al. 2015; Babak et al. 2016; Arzoumanian et al. 2016).

The problem of detecting a GW signal in PTA data is complicated by the variety of noise sources, that can be either peculiar to each pulsars (e.g., spin modifications due to movements in the pulsar crust) or common in all observed systems (e.g., an error in the time standard used as a reference to measure TOAs). The latter are more insidious as they may introduce correlations in the residuals between the timing model and the observed times of arrival. The Hellings and Downs curve describes the cross-correlation due to an isotropic GW background between pairs of pulsars as a function of

* E-mail: jgoldstein@star.sr.bham.ac.uk

their angular separation on the sky (Hellings & Downs 1983). Common noise sources such as errors in the Solar System ephemeris or clock errors also produce cross-correlations between pulsars which may be confused with a GW signal (Tiburzi et al. 2016; Taylor et al. 2017).

Previous approaches to the detection problem have been developed which marginalise over these errors by including uncertainties in the timing model itself. However, these methods are still vulnerable to unmodelled systematics which may remain. For robust detection one would like to have an empirical estimate of the noise with which to compare the observed data. It is difficult to produce such an empirical background distribution due to the finite amount of PTA data available and the fact that the GW signal cannot be removed from the data. This issue has been addressed by the development of techniques to *e.g.* scramble the timing residuals so that the GW-induced cross-correlations are not present in the scrambled data realisation (Taylor et al. 2017).

In this work we investigate an alternative approach applicable to deterministic and individually resolvable signals. Through this method one cancels the gravitational wave signal exactly by exploiting redundancies in the data when the number of data streams exceeds the number of independent degrees of freedom (i.e. the number of polarizations) in the GW signal. Given independent data streams from N detectors and M GW polarizations, one can construct M GW polarization streams and $N - M$ ‘null streams’, which have all GW power from a particular direction removed. This allows a discrimination between GWs and noise which can be used to construct a statistical model of the data. Assuming as working hypothesis that General Relativity holds, only the two tensor polarizations of the GW field are non-vanishing, thus allowing the construction of $N - 2$ null streams.

The null-stream formalism is quite general and has been applied to analyses across the gravitational-wave spectrum. For networks of ground-based detectors the method has been proposed to discriminate between signal and unmodelled noise (Wen & Schutz 2005; Ajith et al. 2006; Chatterji et al. 2006; Rakhmanov 2006). In the context of the Laser Interferometer Space Antenna (LISA) an example of null stream is given by the Sagnac configuration of the detector (Amaro-Seoane et al. 2017), in which the interferometer channel are combined to cancel out GW signals, thus serving as detector calibrator to assess the instrumental noise level (Shaddock 2004). Recently, Zhu et al. (2015, 2016) adapted those techniques to PTAs, and investigated the benefits of using null streams to reconstruct the GW signal properties and quantify detection confidence in a frequentist framework.

Here we develop a Bayesian PTA analysis using the null-stream formalism for an arbitrary deterministic GW source. We derive the associated likelihood function and use it for the recovery of the source properties. Although the null-stream formalism works in both the time and frequency domains given appropriate interpolation, for simplicity we consider the frequency domain analysis of simulated data containing a monochromatic GW source from a supermassive black hole binary (Hazboun & Larson 2016).

As a first application of the method, we investigate its performance in localising resolvable SMBHBs. Sky localisation is of paramount importance for PTA science, because it opens the possibility of identifying the source galactic host and of looking for possible electromagnetic counterparts; consequently it has been tackled by several authors in recent years (Sesana & Vecchio 2010; Lee et al. 2011; Babak & Sesana 2012; Ellis et al. 2012; Taylor et al. 2014; Zhu et al. 2015, 2016; Wang & Mohanty 2017). For this specific problem, the null stream technique is expected to pro-

duce equivalent results to other analysis methods (exploiting a linear transformation on the data). However, this application serves to lay out the formalism in the Bayesian framework. This will be used in future work to exploit the main advantage of null streams: by creating combinations of data that contain noise only, they are a powerful tool to discriminate signal from noise, thus allowing to tackle the issue of detection confidence, which is critical in PTA data analysis (Taylor et al. 2017). We perform a systematic investigation of the source sky localisation as a function of signal-to-noise ratio (SNR) and number of pulsars in the array. We then consider the case of a detection with current PTAs, demonstrating the great benefits of combining regional PTA data under the aegis of IPTA.

The paper is organized as follows. In Sec. 2 we describe the null-stream construction and the Bayesian framework employed to extract source properties from the data. In Sec. 3 we investigate systematically the scaling of source sky localisation capabilities as a function of the main PTA parameters and compare our results with previous work based on the Fisher Matrix approximation. In Sec. 4 we apply our techniques to current PTAs and demonstrate the benefit of the world-wide IPTA network. We summarize our main findings and discuss future prospects for expanding this work in Sec. 5.

2 METHOD

The basic idea behind the null stream method is the following: data is obtained from N detectors that have a linear response to a GW signal. The two polarizations of the GW can be reconstructed from the detector output, which leaves the possibility to construct an additional $N - 2$ independent data combinations. If the detector responses are known, these combinations can be made such that any GW signal is cancelled out, leaving only noise, hence the name null streams.

The following sections will explain in detail the construction of null streams for Pulsar Timing Array (PTA) data (Sec. 2.2) and our choice of a continuous wave signal (Sec. 2.3). Then, the use of null streams in the sky localisation of a single source GW signal (Sec. 2.4) and the implementation for discrete data (Sec. 2.5) are discussed. First in Sec. 2.1, the formalism is set up in terms of the signal and the response of the PTA.

2.1 Response of a PTA

Assume we have a plane wave propagating in the direction $\hat{\Omega}$, with angular frequency ω . A coordinate system can be chosen by using $\hat{\Omega}$ and two additional orthonormal vectors:

$$\begin{aligned}\hat{\Omega} &= (\sin \theta \cos \phi, \sin \theta \sin \phi, \cos \theta) \\ \hat{m} &= (\sin \phi, -\cos \phi, 0) \\ \hat{n} &= (\cos \theta \cos \phi, \cos \theta \sin \phi, -\sin \theta).\end{aligned}\quad (1)$$

Here, θ and ϕ are the polar sky coordinates of the direction of propagation of the GW ($-\hat{\Omega}$ points towards the source). The two orthogonal polarizations of the gravitational wave can be written in terms of the $+$ and \times transverse basis tensors

$$\begin{aligned}e_{ij}^+(\hat{\Omega}) &= \hat{m}_i \hat{m}_j - \hat{n}_i \hat{n}_j \\ e_{ij}^\times(\hat{\Omega}) &= \hat{m}_i \hat{n}_j + \hat{n}_i \hat{m}_j.\end{aligned}\quad (2)$$

The metric perturbation due to the GW then, is given by:

$$h_{ij}(t) = h^+(t)e_{ij}^+ + h^\times(t)e_{ij}^\times, \quad (3)$$

where $h^+(t)$ and $h^\times(t)$ are the amplitudes of the two polarizations.

A GW propagating through the Galaxy affects the travel time of radio emission travelling from a pulsar to the Earth. The resulting redshift in the pulse TOAs depends on the relative angle between the pulsar, in direction $\hat{\mathbf{p}}$, and the GW propagation direction $\hat{\mathbf{\Omega}}$ (see, e.g., Anholm et al. 2009; Lee et al. 2011).

$$z(t, \hat{\mathbf{\Omega}}) = \frac{1}{2} \frac{\hat{p}^i \hat{p}^j}{1 + \hat{\mathbf{\Omega}} \cdot \hat{\mathbf{p}}} \Delta h_{ij}, \quad (4)$$

where $\Delta h_{ij} = h_{ij}(t_E, \hat{\mathbf{\Omega}}) - h_{ij}(t_p, \hat{\mathbf{\Omega}})$, being $h_{ij}(t_p)$ and $h_{ij}(t_E)$ the metric perturbation at the pulsar at the time of pulse emission and at the Earth at the time of pulse detection, respectively. Only the Earth term adds up coherently in the analysis of multiple pulsars in the array. Therefore, for any burst-like signal with duration shorter than the travel time of the pulses only the Earth term is relevant. For a continuous wave (e.g. from a SMBHB) on the other hand, the pulsar term is present, although its frequency may differ slightly from that of the Earth term as it samples different periods in the wave-train of the slow inspiral (Babak et al. 2016). Whether the pulsar and the Earth terms fall at different frequencies or not depends on the intrinsic properties of the GW source, the distance to the pulsar and the relative pulsar-source angular separation. Implementing realistic SMBHB population models and considering plausible developments of current PTAs, Rosado et al. (2015) found that either situation is possible, with comparable probability. To simplify the problem, as a first implementation, only the Earth term will be considered in our description of the signal¹. This results in the following definition for the response functions F^+ and F^\times :

$$\begin{aligned} z(t, \hat{\mathbf{\Omega}}) &= \frac{1}{2} \frac{\hat{p}^i \hat{p}^j}{1 + \hat{\mathbf{\Omega}} \cdot \hat{\mathbf{p}}} (h^+(t) e_{ij}^+(\hat{\mathbf{\Omega}}) + h^\times(t) e_{ij}^\times(\hat{\mathbf{\Omega}})) \\ &\equiv F^+(\hat{\mathbf{\Omega}}) h^+(t) + F^\times(\hat{\mathbf{\Omega}}) h^\times(t) \end{aligned} \quad (5)$$

The observables for a PTA are not the redshifts, but the residuals $r(t)$ obtained by taking the difference between the predicted and measured TOAs. The relation between the two is simply that the residuals are the integrated redshifts:

$$r(t) = \int_0^t z(\tau) d\tau. \quad (6)$$

Since the response functions are time independent, applying the integral to the previous Eq. 5 yields:

$$r(t, \hat{\mathbf{\Omega}}) = F^+(\hat{\mathbf{\Omega}}) H^+(t) + F^\times(\hat{\mathbf{\Omega}}) H^\times(t), \quad (7)$$

where $H^+ = \int_0^t h^+(\tau) d\tau$ and similarly for H^\times . Our final calculations will be done in the frequency domain, for which we can substitute $r \rightarrow \tilde{r}$ and $H^+ \rightarrow \tilde{H}^+$, and $H^\times \rightarrow \tilde{H}^\times$, since the Fourier transform is linear.

Eq. 7 can be written for each pulsar in the PTA, resulting in a collection of residuals $\{r_i\}$. Labelling the response functions F_i^+ and F_i^\times for the pulsar in the direction $\hat{\mathbf{p}}_i$, this can be combined into the matrix equation:

$$\mathbf{r} = \begin{pmatrix} F_1^+ & F_1^\times \\ F_2^+ & F_2^\times \\ \vdots & \vdots \\ F_N^+ & F_N^\times \end{pmatrix} \begin{pmatrix} H^+ \\ H^\times \end{pmatrix} \equiv \mathbf{F} \begin{pmatrix} H^+ \\ H^\times \end{pmatrix}, \quad (8)$$

¹ The addition of the pulsar term is, on the other hand, necessary for non evolving sources, and it might also help improving sky localization, as shown by Lee et al. (2011) and Zhu et al. (2016). We will address this case in future work.

where we have defined the response matrix \mathbf{F} . \mathbf{F} depends on the location of the GW source $-\hat{\mathbf{\Omega}}$, but not on the parameters of the specific form of the GW polarizations, which makes the following null stream construction general.

2.2 Null stream construction

For a fixed direction $\hat{\mathbf{\Omega}}$, the matrix \mathbf{F} defines a mapping from the two-dimensional space of gravitational waves $\mathbf{H} \equiv (H^+, H^\times) \in \mathbb{R}^2$ to the N -dimensional space of residuals from N pulsars in the array. The image of this mapping contains the residuals induced by a gravitational wave, but the measured response data $\mathbf{d} \in \mathbb{D}$ is subject to additional noise \mathbf{n} such that $\mathbf{d} = \mathbf{F}\mathbf{H} + \mathbf{n}$. For $N > 2$, the space \mathbb{D} can be split into a two-dimensional subspace with the image of \mathbf{F} , and an orthogonal $N - 2$ -dimensional subspace. This second subspace – the nullspace \mathbb{A} – is spanned by a set of $N - 2$ independent null-streams, that are also independent of the gravitational wave.

There are different ways to choose the $N - 2$ independent null streams from detectors' output \mathbf{d} (e.g. Zhu et al. (2015, 2016) use a different method than us). However, it is possible to impose the more stringent requirement that the null streams are orthogonal. The method that we describe here has been adapted from work by Chatterji et al. (2006) and Rakhmanov (2006). In short, it's a construction of a set of orthogonal basis vectors for the nullspace \mathbb{A} .

We are interested in inverting the mapping \mathbf{F} from gravitational-waves to a given set of residual data so that we may reconstruct the signal and find the null-streams. The maximum likelihood solution for \mathbf{H} is given by $\hat{\mathbf{H}} = \mathbf{F}_{MP}^{-1} \mathbf{d}$, where $\mathbf{F}_{MP}^{-1} \equiv (\mathbf{F}^T \mathbf{F})^{-1} \mathbf{F}^T$ is the Moore-Penrose pseudo-inverse of \mathbf{F} (Rakhmanov 2006). This can be seen as a projection of the data onto the two dimensional subspace of \mathbb{D} spanned by the column vectors \mathbf{F}^+ and \mathbf{F}^\times of the response matrix \mathbf{F} . The null streams are found by projecting onto the orthogonal space \mathbb{A} , to ensure the null-streams contain no component of the signal. Say a basis for the null space is $\{\hat{\mathbf{e}}_i\}$, with $\hat{\mathbf{e}}_i \cdot \mathbf{F}^+ = \hat{\mathbf{e}}_i \cdot \mathbf{F}^\times = 0$ where $i \in 1, \dots, N - 2$ labels the basis vectors. Then the matrix \mathbf{A} with rows $\hat{\mathbf{e}}_i^T$ is the nullspace projection matrix because $\mathbf{A}\mathbf{F} = \mathbf{0}$ as per construction (where $\mathbf{0}$ is a $(N - 2) \times 2$ zero matrix). The $N - 2$ null streams can then be calculated as:

$$\mathbf{A}\mathbf{d} = \mathbf{A}(\mathbf{F} \begin{pmatrix} H^+ \\ H^\times \end{pmatrix} + \mathbf{n}) = \boldsymbol{\eta} + \mathbf{A}\mathbf{n}. \quad (9)$$

Here we define $\boldsymbol{\eta}$ to be the vector of null streams which all equal zero ($\eta_i = 0$).

To find the basis $\{\hat{\mathbf{e}}_i\}$, consider the projection operators $\mathbf{P} = \mathbf{F}\mathbf{F}_{MP}^{-1}$, and $\mathbf{S} = \mathbf{I} - \mathbf{P}$, where \mathbf{I} is the $(N \times N)$ identity matrix (see also Rakhmanov 2006). The first projects onto the column space:

$$\mathbf{P}\mathbf{F} = \mathbf{F}\mathbf{F}_{MP}^{-1}\mathbf{F} = \mathbf{F}, \quad (10)$$

and the second onto the null space:

$$\mathbf{S}\mathbf{F} = (\mathbf{I} - \mathbf{P})\mathbf{F} = \mathbf{F} - \mathbf{F} = \mathbf{0}. \quad (11)$$

However, \mathbf{S} is an $(N \times N)$ matrix whereas the null space only has $N - 2$ dimensions. A way to reduce \mathbf{S} to $((N - 2) \times N)$ is to use the QR-decomposition, which yields $\mathbf{S} = \mathbf{Q}\mathbf{R}$. Then, if \mathbf{S} has rank r , the first r columns of \mathbf{Q} form an orthonormal basis for the column vectors of \mathbf{S} . Therefore, the first $N - 2$ columns of \mathbf{Q} form the basis $\{\hat{\mathbf{e}}_i\}$ that we were looking for.

² We drop the dependence on time as the logic applies to any particular time stamp (or Fourier frequency bin when using $\hat{\mathbf{H}}$).

Because both the reconstructed GW polarizations and the null streams are informative, the projectors F_{MP}^{-1} and A are combined in the square matrix M . The total projection of the data with M is:

$$M\mathbf{d} = \begin{pmatrix} (F_{MP}^{-1})_1 \\ (F_{MP}^{-1})_2 \\ \hat{e}_1 \\ \vdots \\ \hat{e}_{N-2} \end{pmatrix} \left(F \begin{pmatrix} H^+ \\ H^\times \end{pmatrix} + \mathbf{n} \right) = \begin{pmatrix} H^+ \\ H^\times \\ \eta_1 \\ \vdots \\ \eta_{N-2} \end{pmatrix} + M\mathbf{n} \quad (12)$$

$$\equiv \mathbf{h} + M\mathbf{n}, \quad (13)$$

where we have defined \mathbf{h} as the combined vector of GW polarizations and null streams.

2.3 Continuous wave signal

The null stream method can be used with any assumption on the functional form of the GW polarizations $h^+(t)$ and $h^\times(t)$. Here we specialise and assume the signal to take the form of a monochromatic continuous wave from a circular SMBHB. The monochromatic assumption is valid so long as the SMBHB is light enough such that any frequency evolution over the time scale of the observation is negligible, which is generally true for relevant systems (Sesana & Vecchio 2010; Taylor et al. 2016). Both polarizations h^+ and h^\times are related, via the angle ψ , to the GW signal emitted by the source:

$$h^+(t) = A^+ \langle \boldsymbol{\lambda} \rangle \cos(2\psi) - A^\times \langle \boldsymbol{\lambda} \rangle \sin(2\psi) \quad (14)$$

$$h^\times(t) = A^+ \langle \boldsymbol{\lambda} \rangle \sin(2\psi) + A^\times \langle \boldsymbol{\lambda} \rangle \cos(2\psi), \quad (15)$$

where

$$A^+ = A \frac{1}{2} (1 + \cos^2 t) \cos(\omega_0 t + \phi) \quad (16)$$

$$A^\times = A \cos t \sin(\omega_0 t + \phi). \quad (17)$$

The frequency of the GW is $f_0 = \omega_0/2\pi$ (which is twice the orbital frequency). For a chosen frequency and sky position, the remaining parameters of the source are the binary's orbital inclination t , the polarization angle ψ , the phase offset ϕ and the amplitude A , which we encapsulate in the parameter vector $\boldsymbol{\lambda}$. The amplitude depends on the physical parameters of the SMBHB:

$$A = \frac{4\mathcal{M}(\pi f_0)^{2/3}}{D_l}, \quad (18)$$

where \mathcal{M} is the redshifted chirp mass of the binary, D_l the luminosity distance to the source and f_0 the observed GW frequency (here $G = c = 1$). However in this work, we treat A as an overall scaling factor of the signal.

The form of the signal needs to be changed when considering the PTA residuals instead of the redshifts, as in Eq. 7. Applying the time integral to Eqs. 16 and 17 yields:

$$A_{(t)}^+ \equiv \int_0^t A^+(\tau) d\tau = \frac{A}{2\omega_0} (1 + \cos^2 t) \sin(\omega_0 t + \phi) \quad (19)$$

$$A_{(t)}^\times \equiv \int_0^t A^\times(\tau) d\tau = -\frac{A}{\omega_0} \cos t \cos(\omega_0 t + \phi), \quad (20)$$

where we disregard constants of the integration.

2.4 Localisation

The predictable shape of the null streams (they contain only noise) can have many applications. For example, the null stream statistic should follow the statistic of the noise and can therefore be used

to validate candidate GW signals and assess detection confidence, which we plan to investigate in the future. In this work, we use it to estimate the sky location of a GW source. Only when constructing the response function and the matrix M using the correct sky location, do the signal components in the null streams cancel out. Thus, an estimate for the sky location is obtained by varying $\hat{\boldsymbol{\Omega}}$ until the null streams are closest to zero (and, consequently, the GW polarizations closely match the model).

To quantify this, consider the posterior distribution on the sky location, under the assumption \mathcal{H}_{sig} that a signal is present:

$$p(\hat{\boldsymbol{\Omega}}|\mathbf{d}, \mathcal{H}_{sig}) = \frac{p(\hat{\boldsymbol{\Omega}}|\mathcal{H}_{sig})p(\mathbf{d}|\hat{\boldsymbol{\Omega}}, \mathcal{H}_{sig})}{p(\mathbf{d})}. \quad (21)$$

The prior on the sky location $p(\hat{\boldsymbol{\Omega}}|\mathcal{H}_{sig})$ is assumed to be flat. To calculate the likelihood, a model for the data is needed. In the presence of a signal and additive Gaussian noise, Eq. 13 describes what is needed: $\mathbf{d} = M^{-1}\mathbf{h} + \mathbf{n}$. This naturally leads to the Gaussian log-likelihood function:

$$l = -\frac{1}{2} \left((\mathbf{d} - M^{-1}\mathbf{h})^\top \Gamma (\mathbf{d} - M^{-1}\mathbf{h}) \right) + norm. \quad (22)$$

where Γ is the inverse of the covariance matrix appropriate for the expected noise of the detector. The normalisation is not written explicitly, as the likelihoods are normalised numerically as a last step in the calculation. Eq. 22 can be rewritten using $\mathbf{l} = M^{-1}\mathbf{M}$ to the following form:

$$l = -\frac{1}{2} \left((M\mathbf{d} - \mathbf{h})^\top ((M^{-1})^\top \Gamma M^{-1}) (M\mathbf{d} - \mathbf{h}) \right) + norm. \quad (23)$$

The $M^{-1}\mathbf{h}$ term in Eq. 22 depends on both the sky location $\boldsymbol{\Omega}$ through M and the GW model parameters $\boldsymbol{\lambda}$ through \mathbf{h} . In Eq. 23 these dependencies are split up over the terms $M\mathbf{d}$ and \mathbf{h} , which simplifies calculations.

To obtain the likelihood $p(\mathbf{d}|\hat{\boldsymbol{\Omega}}, \mathcal{H}_{sig})$, this l is marginalised over the GW parameters $\boldsymbol{\lambda}$. By having split the dependency on $\boldsymbol{\lambda}$ from $M\mathbf{d}$, this quantity has to be calculated only once for each sky location. For our choice of a continuous wave signal in Section 2.3, the marginalization is done with a combination of an analytical and numerical integration. A benefit to the particular method of null stream construction used (Sec. 2.2) becomes apparent here. For a diagonal covariance matrix Γ^{-1} of the detector noise, the transformed matrix $(M^{-1})^\top \Gamma M^{-1}$ is largely kept diagonal (except for the covariance between the GW polarization amplitudes in the first two entries of $M\mathbf{d}$ and of \mathbf{h}), which can make the numerical computation more efficient.

To quantify how well a GW source is localised, we define Ω_{90} as the fraction of the sky area containing 90% of the likelihood. This quantity can be expressed as a fraction of the sky or in square degrees (since the whole sky is 4π , sr. $\approx 4.1 \times 10^4$ deg²).

2.5 Discrete data

One draw-back of the null-stream construction is that it requires the ability to take linear combinations of the data at a particular time or frequency. In practice, PTA residuals are not observed at the same time for each pulsar, so an interpolation in time or frequency is required to use this method on real data. In the following, we make the simplifying assumption that we can work with Fourier transformed quantities \tilde{h}^+ and \tilde{h}^\times .

Any PTA observations will be discrete in time, and so is our simulated data. As a simplification, the simulation has n data points

evenly spaced in time, with cadence Δt . This allows for calculating the discrete Fourier transform efficiently with the Fast Fourier Transform (FFT) algorithm (Cooley & Tukey 1965). In the case of unevenly sampled data, interpolation methods can be used to estimate residuals at evenly sampled timestamps, allowing the calculation of the Fourier transform. This was addressed, for example, by Zhu et al. (2015), who used linear interpolation between data-points. Alternatively, Fourier coefficients for an arbitrary basis of frequencies can be directly estimated via a likelihood calculation for any type of data, as demonstrated in Lentati et al. (2013).

For the study of sky localisation with the null stream method, the assumption is made that a source has been detected at a known frequency f_0 . Therefore, the likelihood calculation can be restricted to the Fourier component at this frequency. To speed up the calculation, the number of points and cadence is matched such that there is only one non-zero Fourier component. This is effected when Δt is a multiple of $(nf_0)^{-1}$, in which case bin number $f_0/\Delta f = f_0 n \Delta t$ completely contains the signal power. In general, the power in a discrete Fourier transformed is spread over multiple bins and can still be recovered.

The model for the GW polarizations from Eqs. 19 and 20 needs to be adapted to Fourier-transformed discrete data. The transform of the sine and cosine functions are delta functions, which yield a contribution at $f = -f_0$ and $f = f_0$ when integrated over frequency. The first can be disregarded since we only have positive frequencies. In the discrete transform, this power will end up spread over the bin corresponding to f_0 , and so there is an additional factor $1/\Delta f = T$. The model then, is:

$$\tilde{A}_{(t)}^+(f_0) \approx T \frac{A}{4\omega_0} (1 + \cos^2 t) e^{i(3\pi/2 + \phi)} \quad (24)$$

$$\tilde{A}_{(t)}^\times(f_0) \approx T \frac{A}{2\omega_0} (\cos t) e^{i(\pi + \phi)}. \quad (25)$$

The full model is $\mathbf{h} = (\tilde{H}^+, \tilde{H}^\times, 0, \dots, 0)$ (see Eq. 13). As such, the model can be written as $\mathbf{h} = \mathbf{h}_0 e^{i\phi}$, which means that the likelihood from Eq. 23 can be analytically marginalised over the phase ϕ (from 0 to 2π) (e.g. Jaranowski & Krolak (2010)). Without explicitly writing the normalisation, the marginalised likelihood is given by:

$$p(\mathbf{M}\mathbf{d}|\hat{\mathbf{\Omega}}, \boldsymbol{\lambda}, \boldsymbol{\psi}, \mathcal{H}_{sig}) = \int_0^{2\pi} d\phi p(\phi|\mathcal{H}_{sig}) p(\mathbf{M}\mathbf{d}|\phi, \hat{\mathbf{\Omega}}, \boldsymbol{\lambda}, \boldsymbol{\psi}, \mathcal{H}_{sig}) \\ \propto \exp\left(-\frac{1}{2}(|\mathbf{M}\mathbf{d}|^2 + |\mathbf{h}_0|^2)\right) I_0(|\mathbf{M}\mathbf{d} \cdot \mathbf{h}_0|). \quad (26)$$

Here, the dot product and norm is analogous to the product in Eq. 23, which is weighted by the transformed inverse covariance matrix: $a \cdot b = a^\top ((\mathbf{M}^{-1})^\top \Gamma \mathbf{M}^{-1}) b$. The last term in Eq. 26 is the modified Bessel function of the first kind I_0 .

The other parameters of the SMBHB A , $\boldsymbol{\psi}$ and t can not be marginalised analytically. To get the likelihood for a specific sky location, $p(\mathbf{M}\mathbf{d}|\hat{\mathbf{\Omega}}, \mathcal{H}_{sig})$, the other parameters are marginalised numerically. This is a three dimensional integral over prior ranges $0 - \pi$ for $\boldsymbol{\psi}$ and $0 - 10^{-12}$ for A . The prior for the inclination is flat in $\cos t$, with a range -1 to 1 .

3 RESULTS: SKY LOCALISATION PERFORMANCE

To investigate the performance of our localisation method, we ran a set of simulations in which a GW signal according to the SMBHB model (Eqs. 16 and 17) is added to white noise. The likelihood as in Eq. 23 is then calculated over a grid of sky locations, and

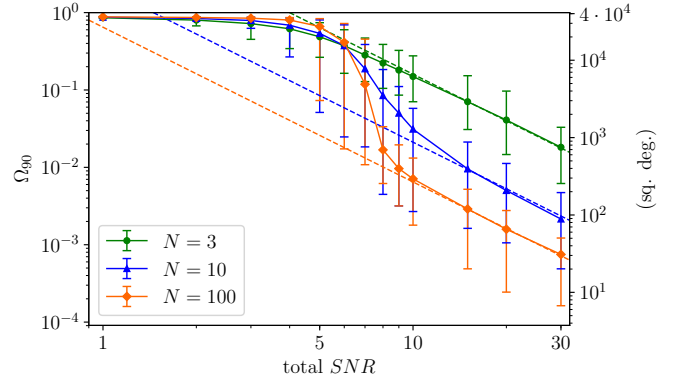


Figure 1. Fraction of the sky area containing 90% of the likelihood (Ω_{90}) vs total SNR. Data points show the mean value of 10 random realisations of a PTA with $N = 3, 10$ and 100 pulsars, with the errorbars showing the total span of results (from minimum to maximum). A power law $\Omega_{90} \propto (SNR)^{-2}$ is fitted to the last three points of each curve. For visibility, not all PTA sizes are plotted, but curves without errorbars are shown in Fig. 2.

marginalised over the model parameters, to determine Ω_{90} . This grid consists of 12 288 equal area pixels made using the HEALpix algorithm (Górski et al. 2005) via healpy³.

Simulations were carried out with a varying number of pulsars N in the PTA, and over a range of SNRs. For N , the values 3, 5, 10, 20, 30, 50 and 100 were chosen. To construct at least one null stream, 3 is the minimum number of pulsars needed, whereas 50 is about the number of pulsars in the combined data set of the current PTA observatories, the International Pulsar Timing Array (IPTA) (Verbiest et al. 2016). However, IPTA pulsars are not all equally good timers and most of the information is carried by the ~ 10 best ones. In this respect, an array with $N = 50$ good timers is more comparable to what might be achieved in the future with the Square Kilometer Array (SKA, see Janssen et al. 2015). The range of SNR values used is 1 to 30. This is the cumulative SNR in the PTA, i.e. summed over the pulsars:

$$SNR^2 = \sum_{p=1}^N \sum_{i=0}^{n-1} \frac{r_{i,p}^2}{\sigma_p^2}. \quad (27)$$

Here, $\{r_{i,p}\}$ is the time series of n residuals from pulsar p . The noise model consists of white noise in the residuals with rms σ_p for each pulsar. All σ_p are set to 100 ns.⁴ To fix the SNR to a given value, the amplitude of the injected GW is adjusted accordingly.

For each pair of N and SNR values, 10 simulations were performed injecting a GW source at $\theta = \pi/2, \phi = 0$, with a frequency of 20 nHz, and pulsars at randomised locations (with a uniform prior over the sky). These random choices are seeded such that for a given N , for each SNR the same 10 PTA configurations are used. 300 data points were simulated with a cadence of 10^6 s, such that the data contain 6 full cycles of the GW signal.

3.1 Scaling with SNR at fixed N

We investigate the sky localisation as a function of the two main parameters identifying the detection, namely the SNR and the number

³ healpy.readthedocs.io

⁴ A more sophisticated noise model could be used by taking the product $r_i \Gamma_{ij} r_j$ with an inverse covariance matrix Γ .

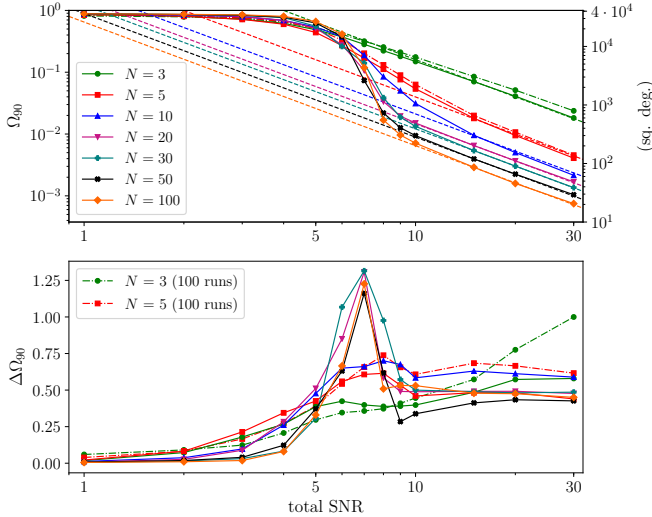


Figure 2. Top panel: Fraction of the sky area containing 90% of the likelihood (Ω_{90}) vs total SNR, as in Fig. 1. Bottom panel: Standard deviation normalised by the mean in the 10 realisations used for each point in the top panel. Dashed lines represent values as obtained with a re-run of 100 realisations.

of pulsars in the array. Here we fix N and vary SNR and in the following Sec. 3.2 we will fix SNR and vary N . In Fig. 1, the results for $N = 3, 10$ and 100 are shown with points referring to the mean Ω_{90} and error bars spanning the range of results in the 10 simulations for each data point. At low SNR, Ω_{90} is limited to 90% of the sky, as there is no information gained from the data. For $5 < \text{SNR} < 10$ data become informative and the sky localization rapidly improves, eventually converging to a $\Omega_{90} \propto (\text{SNR})^{-2}$ relation at high SNR. This has to be expected since at high SNR the likelihood surface can be approximated by a multivariate Gaussian around the true value of the source parameters (Vallisneri 2008). Parameter determination then follow the theoretical scaling $\Delta\lambda \propto (\text{SNR})^{-1}$. Sky localization is given by a combination of the two angle parameters θ and ϕ (or equivalently right ascension and declination), therefore the scaling $\Omega_{90} \propto (\text{SNR})^{-2}$ is recovered.

In the region around SNR from ~ 5 to ~ 10 , a transition occurs between the two regimes (from non-informative to informative data). In Fig. 2, the medians of the 10 runs for all values of N are plotted, along with the spread in Ω_{90} in the bottom panel. The transition has a similar behaviour for all N , but the variance around the median value is much larger for large N . An explanation is that for low N the sky localization is still quite poor during the transition; regardless of the pulsar configuration, Ω_{90} contains a significant fraction of the sky, as shown in Fig. A1 for the case $N = 3$. Conversely, for large N the information carried by the data in the transition region strongly depends on the specific pulsar location, as shown in Fig. A2 for the case $N = 30$. Here we see that when some pulsars fall close to the source, its sky location is determined to high accuracy despite the low total SNR (e.g. bottom left panel); on the other hand, when there are no pulsars located close to the line of sight to the source, sky localization is poor and Ω_{90} can span as much as half of the sky (e.g. bottom right panel).

3.2 Scaling with N at fixed SNR

The median Ω_{90} as a function of N is shown in Fig. 3 for all investigated SNR. For $\text{SNR} \lesssim 6$ data are not informative and there

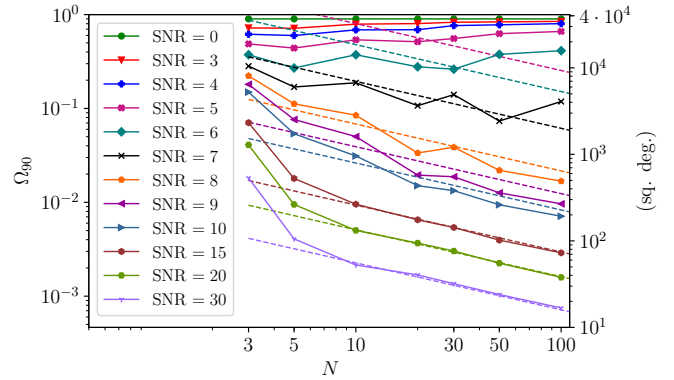


Figure 3. Fraction of the sky area containing 90% of the likelihood (Ω_{90}) vs number of pulsars in the PTA. Data points show the mean value of 10 random realisations of a PTA with total SNR as indicated in the inset label. A power law $\Omega_{90} \propto N^{-1/2}$ is fitted to each curve, ignoring the first two points (with $N = 3$ and 5).

is little dependence of the sky localisation on N . As data become informative for $\text{SNR} \gtrsim 7$, sky localisations benefits from increasing N . In the range $10 \leq N \leq 100$ the improvement in sky localisation precision is well approximated by $\Omega_{90} \propto N^{-1/2}$, especially for the highest SNR investigated.

A possible explanation for this scaling behaviour can be given by the average (over random PTA realizations) angular distance of the closest pulsars to the source. For increasing N , the angular distance between the line of sight to the source and the closest pulsar scales with $N^{-1/2}$ (for uniform randomly distributed pulsars). These closest pulsars contribute most to the sky localization (the antenna patterns are modulated on the smallest scales close to the pulsar).

This conclusion is however non trivial and would need to be tested with $N > 100$. First, sky localization depends on the complex interplay of the antenna beam patterns of all the pulsars contributing to the array. Second, if the total SNR is held fix, not only the distance to the closest pulsar scales with $N^{-1/2}$, but also the SNR contributed by each individual pulsar decreases, so that the $\Omega_{90} \propto N^{-1/2}$ is not obvious. In any case, our systematic study indicates that for foreseeable future detections (involving a realistic number of pulsars up to 100 and SNR in the range 6-to-30) $\Omega_{90} \propto N^{-1/2}$ provides a good empirical fit to the sky localization scaling.

3.3 Dependence on source orientation

So far we considered optimally oriented sources, i.e. face on systems for which the two wave polarizations equally contribute to the signal (cf Eq. (16) and (17)), resulting in a circularly polarized wave. In this case the signal does not depend on the polarization angle, which only adds a contribution to the initial phase offset. Although the sky localization scalings obtained in the previous sections are expected to hold for any source inclination and polarization, the normalization of Ω_{90} might depend on those quantities. To assess this dependence, we proceed as follows. We fix a PTA of 10 pulsars and a source location in the sky. We then perform 100 simulations picking the source parameters from a 10×10 uniform grid in polarization (chosen from $\psi = 0 - 9\pi/20$) and inclinations (chosen from $\cos(i) = 1 - 0$). For this particular experiment, we used noiseless data.

The bottom right panel of Fig. 4 shows the obtained value of Ω_{90} on the aforementioned grid, whereas the bottom left and top

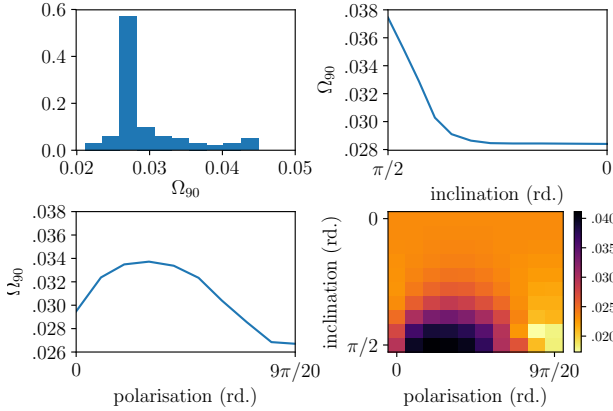


Figure 4. Distribution of sky localisations (Ω_{90}) obtained with varying inclinations and polarization angles of the source. Top left: Normalised histogram of Ω_{90} of all 100 runs. Top right: Distribution of Ω_{90} for varying inclination. Bottom left: Distribution of Ω_{90} for varying polarization angle. Bottom right: All Ω_{90} shown as a colour plot for the grid of polarizations and inclinations used.

right panels show Ω_{90} averaged over inclination and polarization respectively. Firstly, there is essentially no dependence of Ω_{90} on ι and ψ so long as the former is smaller than $\approx \pi/3$. This includes about 50% of all binaries, assuming a uniform source orientation on the sphere. Secondly, the average sky localisation degrades for $\iota > \pi/3$. However, compared to the reference value of $\Omega_{90} = 0.028$ for the face-on case, the worst $\iota - \psi$ combination results in $\Omega_{90} = 0.046$, which is a factor 1.6 worse. The average sky localisation of all the orientations with $\iota > \pi/3$, is only a factor 1.2 worse than the face-on case. We therefore conclude that the sky localisation figures presented in Sec. 3.1 and 3.2 are a fair representation of PTA capabilities for general SMBHBs.

3.4 Comparison with previous results

Our results can be compared to previous studies dealing with systematic investigation of sky localization accuracy as a function of number of pulsars and/or SNR (Sesana & Vecchio 2010; Taylor et al. 2016). Sesana & Vecchio (2010) investigated sky localisation of individual GW sources with PTAs using the Fisher Matrix formalism. Their main result is shown in their Fig. 7, where the sky localisation $\Delta\Omega$ is plotted against SNR and number of pulsars. Although results are overall compatible, there are several differences that are worth highlighting.

First, since they employ the Fisher Matrix formalism, Sesana & Vecchio find a perfect SNR^{-2} scaling down to $SNR = 5$. Our more realistic approach shows that this scaling kicks in only for $SNR \gtrsim 10$, whereas for lower values, sky localization performances are much poorer. For example, at $SNR = 5$ PTAs have essentially no source localisation power and even at $SNR = 7$, typical performances are a factor of ≈ 3 worse than the SNR^{-2} extrapolation. This is particularly relevant since the signal builds up slowly with time, which means that the first confident single source PTA detection will necessary have low SNR. PTAs will therefore have limited capabilities to pin down the source parameters in the early stages of detection.

Second, Sesana & Vecchio found that the $N^{-1/2}$ scaling does not hold in general. Their Fig. 7 shows that the sky localisation improvement flattens out for $N > 100$, even though an $N^{-1/2}$ line might provide a reasonable fit in the $10 \leq N \leq 100$ range investi-

gated in this work. It is likely that a saturation point is reached when the average contribution to the SNR of the closest pulsars of order 1. At that point, the signal added in each pulsar (if we keep the total SNR fixed) will be below the typical noise level, and no information about the source sky localisation can be gained.

Third, the normalization of the sky localisation performance is different. For $N = 100$ and $SNR = 10$, Sesana & Vecchio find a median $\Delta\Omega \approx 40\text{deg}^2$, to be compared to our value of about 200deg^2 . This is partly due to the different definition of $\Delta\Omega$, which in their study is the region of the sky with probability $e^{-1} \approx 0.63$ of hosting the source. For a multivariate Gaussian likelihood surface, this area is a factor 2.3 smaller than that enclosing the 90% probability that we use. The 90% probability region of Sesana & Vecchio is therefore $\approx 100\text{deg}^2$, which is only a factor of two smaller than what we find. Fisher Matrix calculation however, provide a lower limit to the sky localisation accuracy. Even for $N = 100$ and $SNR = 10$ we find that the likelihood function is highly non Gaussian, resulting in a slightly worse localisation performance compared to the theoretical limit.

Taylor et al. (2016) constructed a Bayesian pipeline for detection and parameter estimation of *eccentric* binaries and carried out a systematic investigation of parameter errors as a function of SNR. Although the addition of eccentricity increases the complexity of the problem, we do not expect this parameter to couple with the source sky localization, and the results should be comparable with those of our analysis.

The relevant result for comparison is reported in their Fig. 9, that shows $\Delta\Omega$ as a function of SNR for a PTA of 18 pulsars with the properties of those used for the NANOGrav 9-year GW upper limit (Arzoumanian et al. 2016). The trend of $\Delta\Omega$ with SNR is very similar to what we found, showing an initial ‘transition phase’ up to about $SNR \approx 8$, then settling into the SNR^{-2} behavior predicted in the strong signal limit. The overall normalization of the curve is also comparable. At $SNR = 20$, they find a 95% probability region (Ω_{95}) of $\approx 500\text{deg}^2$, which is a factor of a few worse than the Ω_{90} shown in our Fig. 1 for 10 and 20 pulsars, but comparable to the 5 pulsar case. This is likely due to the fact that the 18 pulsars they use are not randomly distributed in the sky and have different noise rms, therefore only the few best contribute significantly to the sky localization. Overall, we deem our results to be in agreement with those of Taylor et al. (2016).

4 IMPLICATIONS FOR CURRENT PULSAR TIMING ARRAYS

The null stream formalism developed in this work can be used to assess sky localisation capabilities of current PTAs. In the previous section, we demonstrated the beneficial effect on sky localisation of higher SNR and larger number of pulsars in the array. The obvious way to increase SNR and number of pulsars is to combine individual PTA datasets under the umbrella of IPTA. In this section we therefore focus on the potential gain of IPTA for individual source localisation.

With the aforementioned goal in mind, we need to compare the capabilities of an IPTA dataset to those of the individual PTA data that went into its production. The only official IPTA data release to date is IPTA DR1, presented in Verbiest et al. (2016). We therefore use:

- EPTA Data Release 1, presented by Desvignes et al. (2016), consisting of 42 MSPs monitored with radio telescopes at Effelsberg, Jodrell Bank, Nancay and Westerbork;

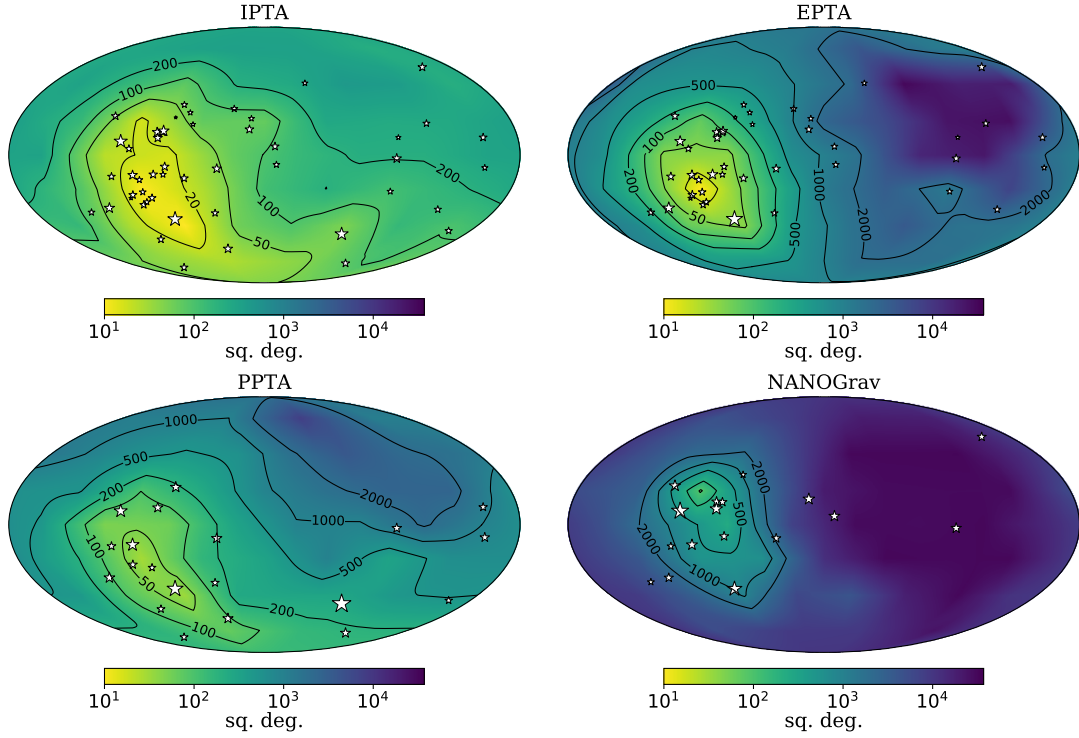


Figure 5. Ω_{90} for a GW source as a function of sky location for IPTA, EPTA, PPTA and NANOGrav. The simulated PTAs are approximates of the IPTA Data Release 1 and its constituent data sets: EPTA DR1, PTPA DR1 and the NANOGrav five year dataset (see text for details). The maps are interpolated from 48 pixels for which a value of Ω_{90} was obtained by placing a GW source with a fixed amplitude ($1.0 \times 10^{-13.5}$) in the middle of that pixel. Contours are plotted at $\Omega_{90} = 20, 50, 100, 200, 500$ and 1000 deg^2 .

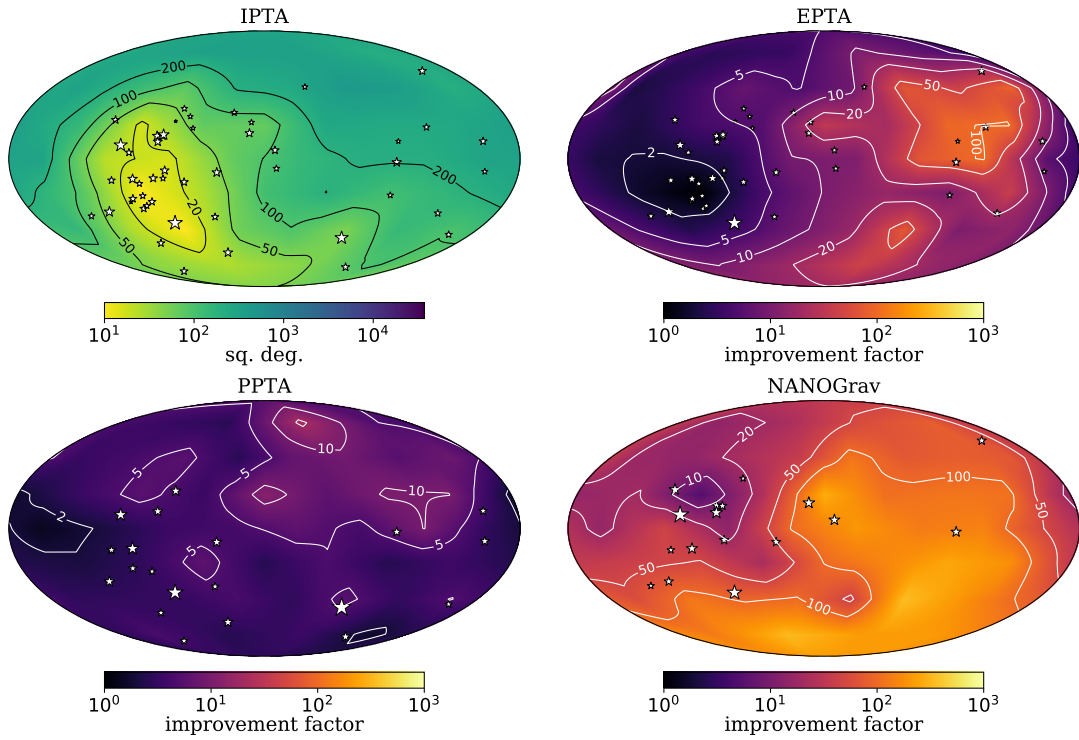


Figure 6. The top left panel is the same as in Fig. 5, whereas the remaining panels show the improvement factor $\mathcal{R}_X(\hat{\Omega})$ of IPTA compared to EPTA, PPTA and NANOGrav (see definition in the main text). The maps are interpolated from 48 pixels, as in Fig. 5. Contours are plotted at $\mathcal{R}_X(\hat{\Omega}) = 2, 5, 10, 20, 50$ and 100 .

PTA	N	\bar{n}	\bar{T} [yr]	SNR	Ω_{90} [deg ²]	\mathcal{R}	$\tilde{\mathcal{R}}$
EPTA	42	592	12.7	19.4	4492	22.0	3.3
PPTA	20	186	6.3	21.8	949	5.0	2.2
NANOGrav	17	50	4.8	8.0	14172	102.2	18.8
IPTA	49	1401	11.1	28.7	167	–	–

Table 1. For each PTA, we list the number of pulsars N , the average number of TOAs per pulsar \bar{n} and the average dataset length \bar{T} . Also listed are the performances of each PTA for a face on source with $A = 10^{-13.5}$ averaged over position in the sky: SNR, sky localization Ω_{90} , and improvement factors \mathcal{R} and $\tilde{\mathcal{R}}$ of IPTA compared to regional PTAs (see text for details).

- the extended PPTA Data Release 1, presented by [Manchester et al. \(2013\)](#), consisting of 20 MSPs monitored with the Parkes radio telescope;
- NANOGrav five year dataset, presented by [Demorest et al. \(2013\)](#), consisting of 17 MSPs, monitored with the Arecibo and Green bank radio telescopes;
- IPTA DR1, presented by [Verbiest et al. \(2016\)](#), consisting of the combination of the three aforementioned datasets, for a total of 49 MSPs.

Several MSPs are monitored by multiple regional PTAs, and so the number of MSPs in IPTA does not correspond to the sum of those in the regional PTAs. However, by combining multiple datasets, IPTA features more high quality pulsars than the regional PTAs. We also stress that we considered the regional PTA data releases that were used to build IPTA DR1, which is the meaningful thing to do since our scope is to assess the benefit of combining PTA data.

The current implementation of our technique allows to use different rms residuals and arbitrary sky location for each individual pulsar, but is only applicable to evenly sampled data spanning the same observation time. We therefore need to modify the PTA data accordingly, while keeping their properties as close as possible to the originals. For each PTA we therefore compute an average dataset length \bar{T} as

$$\bar{T} = \frac{1}{N} \sum_{p=1}^N T_p, \quad (28)$$

where the index p runs over all pulsars in the array and T_p is the dataset length of the p -th pulsar. Likewise, we compute an average number of TOAs per pulsar \bar{n} as

$$\bar{n} = \frac{1}{N} \sum_{p=1}^N n_p, \quad (29)$$

where n_p is the number of TOAs of the p -th pulsar in the array. We then round \bar{n} to the next integer. The values of \bar{T} and \bar{n} for each PTA are given in Table 1. Individual pulsar residual rms values are used as reported in [Desvignes et al. \(2016\)](#) (their Table 1 under rms) for EPTA, in [Manchester et al. \(2013\)](#) (their Table 7 under Rms res.) for PPTA, in [Demorest et al. \(2013\)](#) (their Table 2 under rms) for NANOGrav, and in [Verbiest et al. \(2016\)](#) (their Table 4 under Residual rms) for IPTA.

Now that we have specified the properties of the PTAs, we conduct our experiment by considering a face-on circular SMBHB producing a monochromatic GW signal with frequency $f = 20$ nHz and amplitude $A = 10^{-13.5}$, well within the reach of all PTAs. We place the source in turn at 48 different points in a grid over the sky and use the null stream technique described in Sec. 2 to compute the Ω_{90} sky localisation.

Results are presented in Fig. 5, where contours have been

interpolated over the grid. Firstly, the uneven pulsar distribution in the sky results in a very source position-dependent sky localisation precision. This is particularly true for EPTA and NANOGrav that have localising power mostly in the left side of the map, where all the best pulsars are concentrated, but also for PPTA and IPTA to a lesser extent.

Secondly, the sky localisation performance differs between PTAs. Due to the limited number of good pulsars and of the short data span, the NANOGrav five year dataset performs poorly. EPTA and PPTA on the other hand have comparable capabilities, even though the latter performs better in the right half of the map. The IPTA dataset gives the best localisation overall. The GW source can be localised to better than 20deg² over a region of the sky of about 3500deg² whereas a comparable precision is achieved only by EPTA, on a smaller region of < 1000deg². On the opposite end, IPTA can locate the source to better than 500deg² regardless of its sky location and to better than 200deg² over two thirds of the sky. For comparison, PPTA can locate the source to better than 500deg² in about half of the sky, and in some regions localisation is worse than 2000deg². On average IPTA can localise the source within 167deg² whereas EPTA PPTA and NANOGrav can localise the source within 4492deg² 949deg² and 14172deg², respectively (cf Table 1).

We can then define a relative improvement factor of IPTA sky localisation with respect to regional PTAs as a function of the source location $\hat{\Omega}$ as

$$\mathcal{R}_X(\hat{\Omega}) = \frac{\Omega_{90,\text{IPTA}}(\hat{\Omega})}{\Omega_{90,X}(\hat{\Omega})}, \quad (30)$$

where X stands for EPTA, PPTA or NANOGrav. This relative improvement is shown in Fig. 6. Compared to the best regional dataset (PPTA), sky localisation improves by more than a factor of two virtually everywhere in the sky, and up to a factor of ten in some regions, confirming the superior performance of IPTA.

As shown in Sec. 3 the sky localisation naturally improves as SNR^{-2} , but also (although to a lesser extent) as more pulsars are added to the array, even when keeping the total SNR fixed. We therefore investigate whether the benefits of the combined IPTA datasets go beyond the expected SNR scaling. We define the sky dependent ‘SNR gain normalized’ improvement factor $\tilde{\mathcal{R}}_X(\hat{\Omega})$ as

$$\tilde{\mathcal{R}}_X(\hat{\Omega}) = \mathcal{R}_X(\hat{\Omega}) \times \left(\frac{\text{SNR}_X}{\text{SNR}_{\text{IPTA}}} \right)^2. \quad (31)$$

By normalizing \mathcal{R} with the square of the SNR ratios, $\tilde{\mathcal{R}}$ quantifies the improvement brought by the better IPTA sky coverage. Results are shown in Fig. 7 and highlight that IPTA benefits indeed go beyond the source SNR increment. $\tilde{\mathcal{R}}$ is larger than unity in most of the sky for all regional PTAs. (Exceptions are a fourth, a sixteenth and a forty eighth of the sky for PPTA, EPTA and NANOGrav, respectively. These are the areas where sky localization is best for the regional PTAs). In all cases, gain factors of up to 10 are found in parts of the sky, where the beneficial effect of better sky coverage of IPTA is maximized. Averaged over the sky, we have $\tilde{\mathcal{R}} = 3.3, 2.2, 18.8$ for EPTA, PPTA and NANOGrav respectively, certifying the benefits of IPTA data combination. We remark that the great improvements compared to NANOGrav are simply because only their five year dataset was included in IPTA DR1. An IPTA DR2, including the nine year NANOGrav dataset is currently under construction; this will allow to verify the benefits of IPTA when combining three datasets of comparable quality.

We caution that these results have been obtained by using an average timestamp for all pulsars of each specific array. In practice,

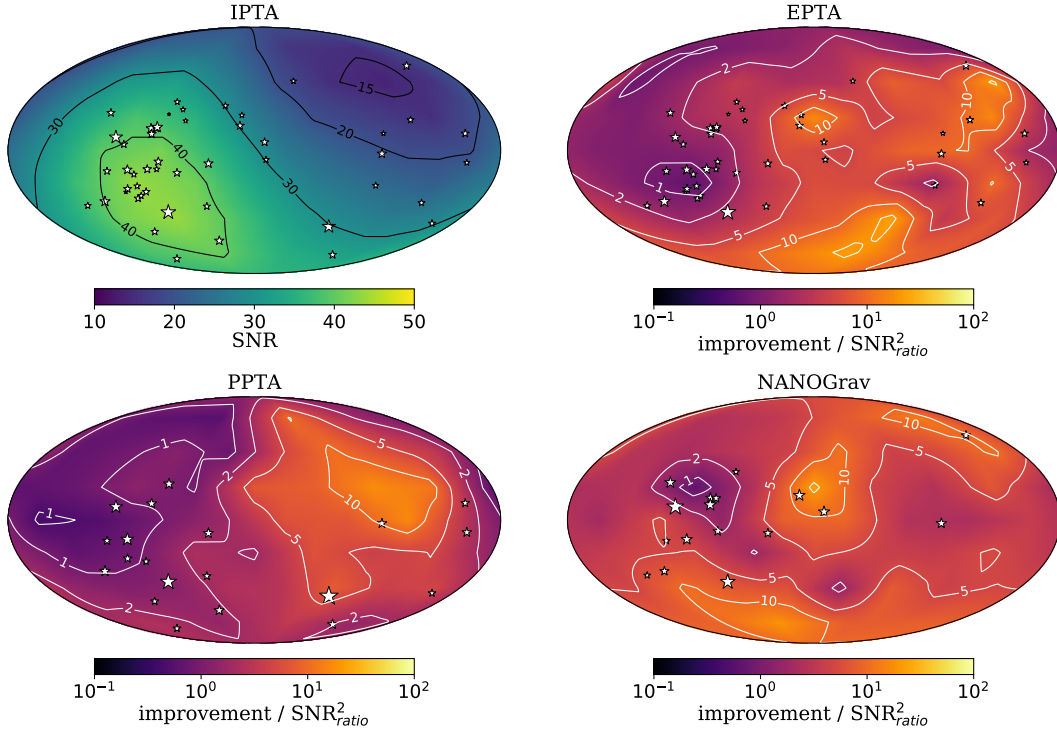


Figure 7. The top left panel shows the source SNR as a function of sky location in the IPTA. The remaining plot show the ‘SNR gain normalized’ improvement factor $\mathcal{R}_X(\hat{\Omega})$ of IPTA compared to EPTA, PPTA and NANOGrav (see definition in the main text). The maps are interpolated from 48 pixels, as in Fig. 5. Contours are plotted at a value of $\mathcal{R}_X(\hat{\Omega}) = 1, 2, 5, 10$ and 20.

PTA data are not evenly sampled and the timespan of observations varies from pulsar to pulsar. We expect, however, that considering more realistic PTAs would only have a minor impact on our conclusions. Here we consider typical resolvable sources at a frequency of several tens of nHz. So long as the cadence of observations is much shorter than the GW period, the assumption of evenly sampled data should not really matter. Furthermore, although the cadence and timespan of individual pulsars are different, they usually lie within a factor of two of the average values that we assumed in Table 1, again suggesting that by using the actual timestamp of each pulsar we should reach similar conclusions. Nonetheless, it is important to verify these expectations by employing an algorithm that can handle the complexity of more realistic datasets, an extension that we plan to explore in future work.

5 CONCLUSIONS

In this paper, we introduced a general mathematical description for the construction of null streams in response of an individual GW source. This method is general, works both in the time and frequency domain and can be applied to any deterministic waveform. We then provided a Bayesian framework to extract the GW source parameters by exploring the likelihood given by the comparison of the constructed null streams and theoretical model. As proof of concept, we applied the method to the special case of a monochromatic GW source generated by a circular SMBHB, considering the Earth term only in the PTA response function. We used this setup to carry out a systematic investigation of PTA sky localization capabilities as a function of the array parameters using the sky region containing

90% of the source location likelihood distribution (Ω_{90}) as figure of merit.

We found that for $SNR \gtrsim 10$, Ω_{90} scales as SNR^{-2} , as expected from theoretical arguments in the high SNR limit. However, we find that at low SNR this scaling breaks down, and the source cannot be well-localised. A transition between the two regimes is found for $5 \lesssim SNR \lesssim 10$, in which the Ω_{90} improvement is much steeper than the theoretical scaling. Ω_{90} is also found to scale as the inverse square root of the number of pulsars in the array $N^{-1/2}$, at least for $10 < N < 100$ and $SNR \gtrsim 8$. As a reference point, the median Ω_{90} for a GW source observed with $SNR = 10$ in an array of 100 equal MSPs randomly distributed in the sky is about 200deg^2 . These results are generally consistent with previous findings based on Fisher Matrix calculation, although there are significant differences in the $5 < SNR < 10$ transition region and in the Ω_{90} normalization.

We then used our formalism to investigate the sky localisation capabilities of regional PTAs compared to IPTA. We found that the benefits of combining data in the IPTA framework go beyond the mere gain in SNR due to the accumulation of a larger amount of data. When normalized by SNR gain, IPTA is found to perform a factor between ~ 2 and ~ 20 better than regional PTAs. This is because combining PTA data provides a better sky coverage and increases the number of high quality pulsars that contribute informative data to the detection. These findings demonstrate that combining regional data under the IPTA umbrella maximises the scientific potential of PTAs as GW detectors.

The framework we applied in this study can be improved in several ways and extended to study a number of problems relevant to PTA data analysis. In particular, our current implementation requires that data are taken at simultaneous times in all pulsars if it were to be

applied to a time-domain analysis. One of our primary future goals is to develop an implementation that can handle arbitrary datasets, with unevenly sampled data, gaps, and different time spans, thus allowing the assembly of a pipeline that can be applied to real data.

We also considered only the Earth term of the GW signal which may or may not be appropriate for the loudest SMBHBs, as shown in Rosado et al. (2015). If the frequency of the pulsar and Earth term cannot be separated, then, while the Earth terms may still be cancelled by the null-stream method, there will remain a contribution to the power from the pulsar terms. This could be treated as an excess unmodelled (noise) power, or may be modelled explicitly by introducing an additional amplitude and phase term for each pulsar. Efficient methods exist to either maximise or marginalize the calculation over these parameters, as shown for example by Zhu et al. (2016) and Taylor et al. (2014), and this is another avenue we wish to explore.

Of great interest is also the expansion of the formalism to treat the cases of multiple deterministic sources and stochastic GW backgrounds. Besides the determination of source parameters, the null stream formalism provides a powerful tool to validate candidate GW signals and assess detection significance, a possibility that we want to explore in the context of Bayesian model selection.

ACKNOWLEDGEMENTS

AS is supported by a University Research Fellow of the Royal Society, and acknowledge the continuous support of colleagues in the EPTA. We thank A. Possenti and S. Taylor for useful comments. JV and AV were supported by UK Science and Technology Facilities Council (STFC) grant ST/K005014/1 and ST/N000633/1, respectively. The methods for this work are implemented using the Python programming language⁵, and make extensive use of the NumPy/SciPy library (Walt et al. 2011; Jones et al. 2001–). Some runs were performed with the University of Birmingham BlueBEAR HPC cluster.

REFERENCES

- Abadie J. et al., 2010, *Classical and Quantum Gravity*, 27, 173001
 Abbott B. P. et al., 2016a, *Physical Review Letters*, 116, 241103
 Abbott B. P. et al., 2016b, *Physical Review Letters*, 116, 061102
 Abbott B. P. et al., 2017, *Physical Review Letters*, 118, 221101
 Ajith P., Hewitson M., Heng I. S., 2006, *Classical and Quantum Gravity*, 23, S741
 Amaro-Seoane P. et al., 2017, *ArXiv e-prints*
 Anholm M., Ballmer S., Creighton J. D. E., Price L. R., Siemens X., 2009, *Phys. Rev.*, D79, 084030
 Arzoumanian Z., et al., 2014, *apj*, 794, 141
 Arzoumanian Z., et al., 2016, *apj*, 821, 13
 Babak S., Sesana A., 2012, *Phys. Rev. D*, 85, 044034
 Babak S., et al., 2016, *mnras*, 455, 1665
 Begelman M. C., Blandford R. D., Rees M. J., 1980, *Nature*, 287, 307
 Chatterji S., Lazzarini A., Stein L., Sutton P. J., Searle A., Tinto M., 2006, *Phys. Rev. D*, 74, 082005
 Chatterji S., Lazzarini A., Stein L., Sutton P. J., Searle A., Tinto M., 2006, *Phys. Rev. D*, 74, 082005
 Colpi M., Sesana A., 2017, *Gravitational Wave Sources in the Era of Multi-Band Gravitational Wave Astronomy*, Augar G., Plagnol E., eds., World Scientific Publishing Co, pp. 43–140
 Cooley J. W., Tukey J. W., 1965, *Mathematics of Computation*, 19, 297

- Demorest P. B. et al., 2013, *ApJ*, 762, 94
 Desvignes G. et al., 2016, *MNRAS*, 458, 3341
 Ellis J. A., Siemens X., Creighton J. D. E., 2012, *ApJ*, 756, 175
 Górski K. M., Hivon E., Banday A. J., Wandelt B. D., Hansen F. K., Reinecke M., Bartelmann M., 2005, *ApJ*, 622, 759
 Hazboun J. S., Larson S. L., 2016, *ArXiv e-prints*
 Hellings R. W., Downs G. S., 1983, *Astrophys. J. Lett.*, 265, L39
 Jaffe A. H., Backer D. C., 2003, *ApJ*, 583, 616
 Janssen G. et al., 2015, *Advancing Astrophysics with the Square Kilometre Array (AASKA14)*, 37
 Jaranowski P., Krolak A., 2010, *Class. Quant. Grav.*, 27, 194015
 Jones E., Oliphant T., Peterson P., et al., 2001–, *SciPy: Open source scientific tools for Python*. [Online; accessed 8 March 2024]
 Lee K. J., Wex N., Kramer M., Stappers B. W., Bassa C. G., Janssen G. H., Karuppusamy R., Smits R., 2011, *MNRAS*, 414, 3251
 Lentati L., Alexander P., Hobson M. P., Taylor S., Gair J., Balan S. T., van Haasteren R., 2013, *Phys. Rev. D*, 87, 104021
 Lentati L., et al., 2015, *mnras*, 453, 2576
 Lorimer D. R., 2008, *Living Reviews in Relativity*, 11
 Manchester R. N. et al., 2013, *Publications of the Astronomical Society of Australia*, 30, e017
 Perrodin D., Sesana A., 2017, *ArXiv e-prints*
 Rajagopal M., Romani R. W., 1995, *ApJ*, 446, 543
 Rakhmanov M., 2006, *Classical and Quantum Gravity*, 23, S673
 Rakhmanov M., 2006, *Class. Quant. Grav.*, 23, S673
 Rosado P. A., Sesana A., Gair J., 2015, *MNRAS*, 451, 2417
 Sazhin M. V., 1978, *Sov. Ast.*, 22, 36
 Sesana A., Vecchio A., 2010, *Phys. Rev. D*, 81, 104008
 Sesana A., Vecchio A., Colacino C. N., 2008, *MNRAS*, 390, 192
 Sesana A., Vecchio A., Volonteri M., 2009, *MNRAS*, 394, 2255
 Shaddock D. A., 2004, *Phys. Rev. D*, 69, 022001
 Shannon R. M., et al., 2015, *Science*, 349, 1522
 Taylor S., Ellis J., Gair J., 2014, *Phys. Rev. D*, 90, 104028
 Taylor S. R., Huerta E. A., Gair J. R., McWilliams S. T., 2016, *Astrophys. J.*, 817, 70
 Taylor S. R., Lentati L., Babak S., Brem P., Gair J. R., Sesana A., Vecchio A., 2017, *Phys. Rev. D*, 95, 042002
 Taylor S. R., et al., 2015, *Physical Review Letters*, 115, 041101
 Tiburzi C. et al., 2016, *MNRAS*, 455, 4339
 Vallisneri M., 2008, *Phys. Rev. D*, 77, 042001
 Verbiest J. P. W. et al., 2016, *Monthly Notices of the Royal Astronomical Society*, 458, 1267
 Walt S. v. d., Colbert S. C., Varoquaux G., 2011, *Computing in Science and Engg.*, 13, 22
 Wang Y., Mohanty S. D., 2017, *Physical Review Letters*, 118, 151104
 Wen L., Schutz B. F., 2005, *Classical and Quantum Gravity*, 22, S1321
 Zhu X.-J. et al., 2015, *MNRAS*, 449, 1650
 Zhu X.-J., Wen L., Xiong J., Xu Y., Wang Y., Mohanty S. D., Hobbs G., Manchester R. N., 2016, *MNRAS*, 461, 1317
 Zhu X.-J., et al., 2014, *mnras*, 444, 3709

This paper has been typeset from a $\text{\TeX}/\text{\LaTeX}$ file prepared by the author.

APPENDIX A: SELECTED SKY MAPS

⁵ www.python.org

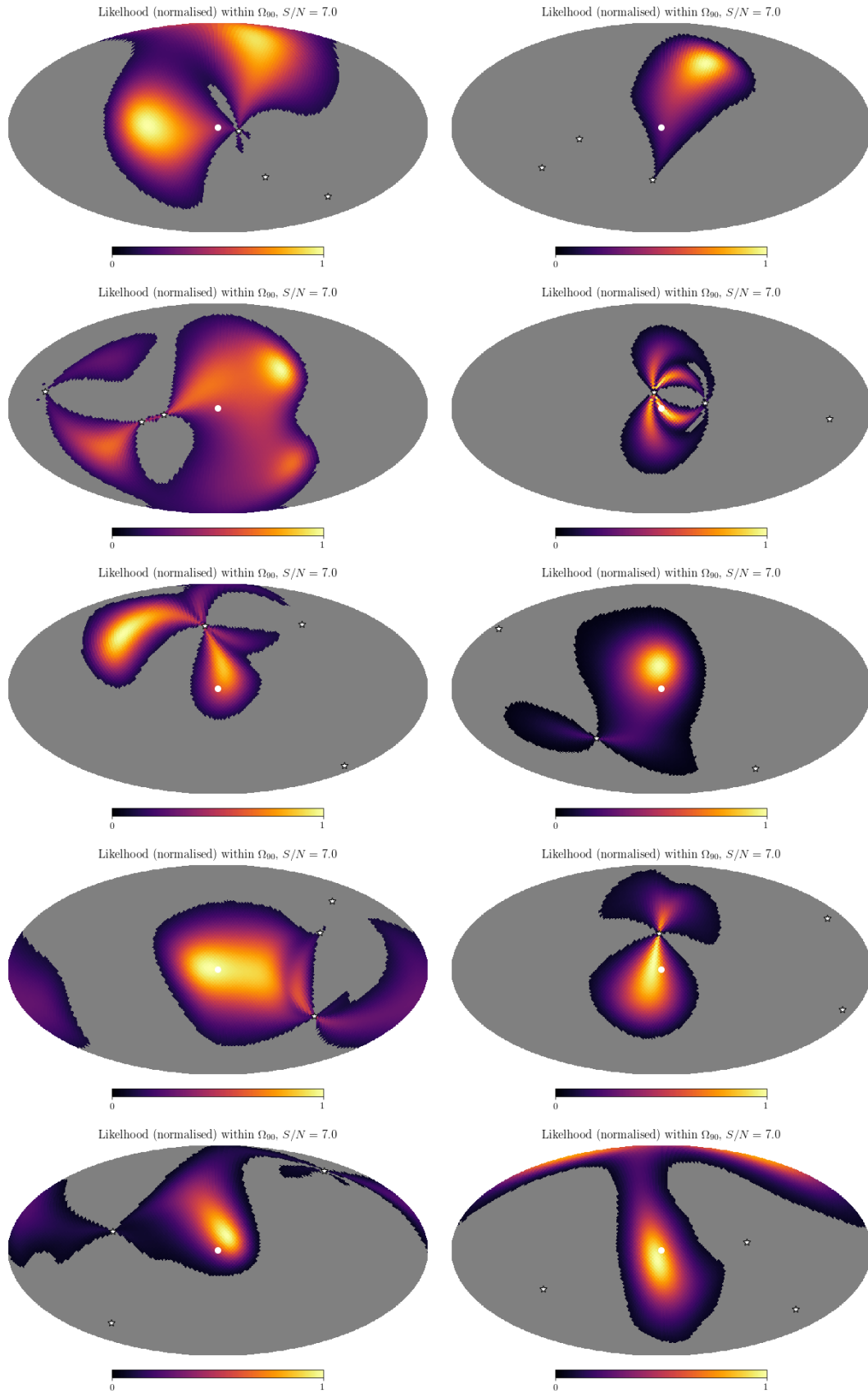


Figure A1. Sky maps of 10 different PTA configurations with 3 pulsars, at a total SNR of 7. The injected source is always located in the middle of the map and indicated with a circle marker. The positions of the pulsars are marked with stars. Pixels not contributing to Ω_{90} are masked in grey. Ω_{90} ranges from 0.143 to 0.469 ($\Delta\Omega_{90} = 0.563$ dex).

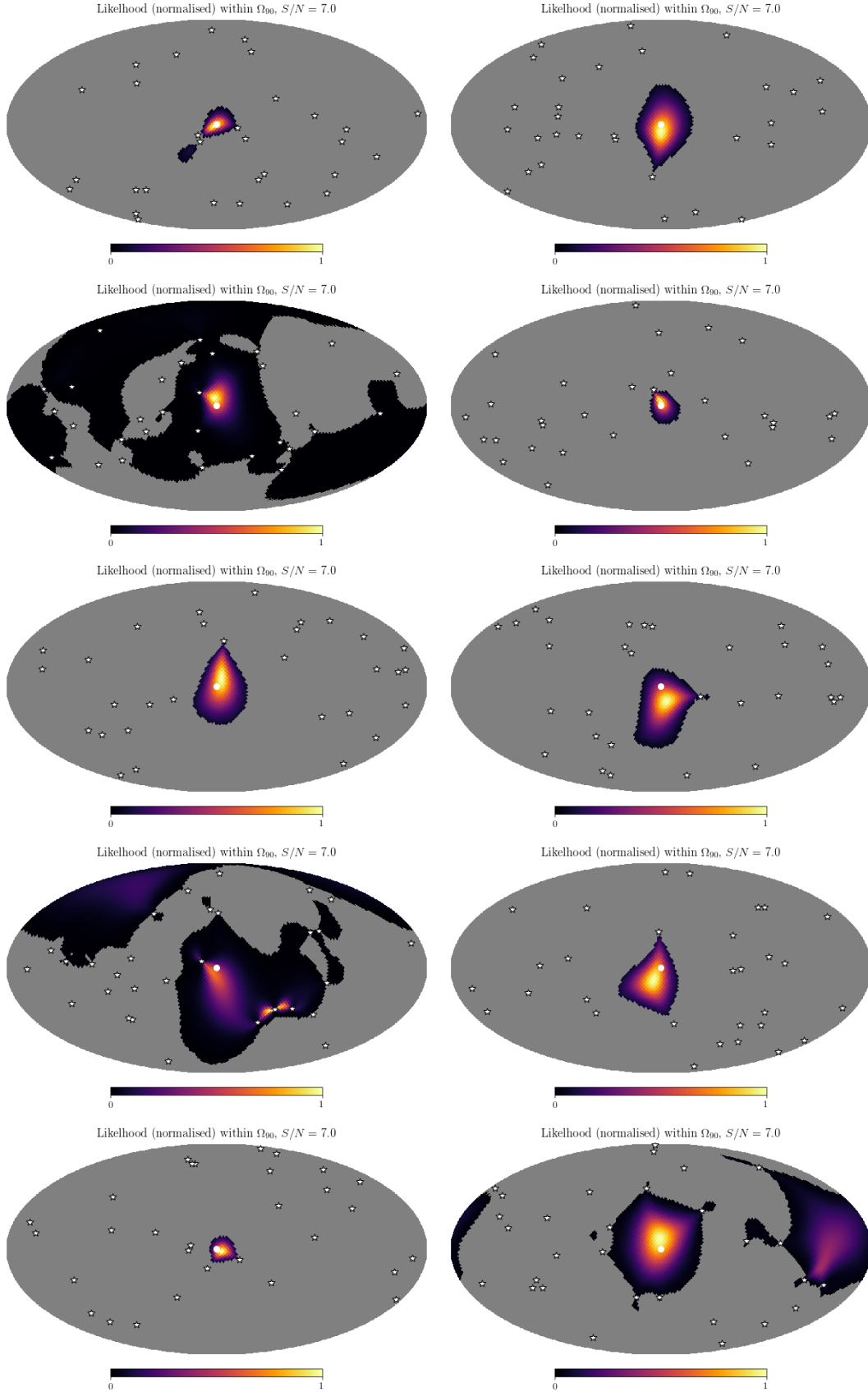


Figure A2. Sky maps of 10 different PTA configurations with 30 pulsars, at a total SNR of 7. The injected source is always located in the middle of the map and indicated with a circle marker. The positions of the pulsars are marked with stars. Pixels not contributing to Ω_{90} are masked in grey. Ω_{90} ranges from 0.0083 to 0.240 ($\Delta\Omega_{90} = 1.84$ dex).